Unfolding of Vortices into Topological Stripes in a Multiferroic Material

X. Wang,[1] M. Mostovoy,[2] M. G. Han,[3] Y. Horibe,[1] T. Aoki,[4] Y. Zhu,[3] and S.-W. Cheong[1,*]
[1]Rutgers Center for Emergent Materials and Department of Physics and Astronomy, Rutgers University, Piscataway, New Jersey 08854, USA
[2]Zernike Institute for Advanced Materials, University of Groningen, Nijenborgh 4, 9747 AG Groningen, The Netherlands
[3]Condensed Matter Physics and Materials Science, Brookhaven National Laboratory, Upton, New York 11973, USA
[4]JEOL USA, Inc., Peabody, Massachusetts 01960, USA

(Received 13 August 2013; revised manuscript received 29 December 2013; published 16 June 2014)

Multiferroic hexagonal $R\mathrm{MnO_3}$ (R = rare earths) crystals exhibit dense networks of vortex lines at which six domain walls merge. While the domain walls can be readily moved with an applied electric field, the vortex cores so far have been impossible to control. Our experiments demonstrate that shear strain induces a Magnus-type force pulling vortices and antivortices in opposite directions and unfolding them into a topological stripe domain state. We discuss the analogy between this effect and the current-driven dynamics of vortices in superconductors and superfluids.

DOI: 10.1103/PhysRevLett.112.247601 PACS numbers: 77.80.Dj, 61.72.-y, 75.60.Ch, 75.85.+t

Understanding and controlling topological defects [1] in ordered states with spontaneously broken symmetries is essential for technological applications of functional materials. For example, ferromagnetic and ferroelectric memory devices rely on field- and current-induced dynamics of domain walls. Unusual physical properties of topological defects open new ways for their manipulation. The electric polarization induced by chiral magnetic domain walls, for example, was used to shift them with an inhomogeneous electric field [2]. Vortices in superfluid liquids and superconductors drift under the influence of the Magnus force in a direction normal to both the supercurrent and vorticity vectors [3,4]. The transverse force also acts on Skyrmions flowing with the electrical current in helimagnetic conductors [5]. Here we show that shear strain has a similar effect on topological defects in multiferroic hexagonal manganites: it moves vortices and antivortices in opposite directions and stabilizes a topological stripe domain state, in which all domain walls have the same chirality.

Hexagonal (h-) $R\mathrm{MnO_3}$ (R = rare earths) are improper ferroelectrics below the transition into a trimerized lattice state caused by the size mismatch between R and Mn-O layers [6–9]. The domains in h-$R\mathrm{MnO_3}$ associated with two polarization directions and three trimerization phases can have two topologically distinct configurations: vortices [10–12] and stripes [13] [see Figs. 1(a) and (b)]. Stripes formed by domain walls spanned over the entire sample are extremely robust, whereas the density of vortices strongly varies depending on heat treatment conditions. When h-$\mathrm{RMnO_3}$ crystals are grown below the ferroelectric-trimerization transition temperature, T_c, which can reach as high as 1450 °C in the case of $\mathrm{LuMnO_3}$, they exhibit stripe domains of large widths. However, when a h-$R\mathrm{MnO_3}$ crystal with stripe domains is heated above and cooled down across T_c, vortex domains form everywhere in the crystal. The density of vortices decreases with the decreasing cooling rate across T_c. Slow relaxational dynamics should eventually expel all vortices from the crystal, leaving possibly stripetype domains [12]. However, unaided by external stimuli, this process takes an astronomically large time, and thus the transformation of vortices into stripes has never been directly observed. Topological characteristics of vortex domains, such as vorticity and $Z_2 \times Z_3$ symmetry, have been discussed in the literature [14,15]. At the same time, the topological nature of stripe domain states and the direct relationship between stripes and vortices have not been explored so far. Here, we report the direct observation of the vortex-to-stripe transformation in the presence of shear strain with a gradient, unveiling the topological nature of stripes. We show that strain is an effective tool for vortex control: previously only domain walls could be moved with an applied electric field, while the vortex cores remained unaffected [15–17].

Platelike hexagonal $\mathrm{ErMnO_3}$ single crystals ($\sim 1 \times 1 \times 0.02\ \mathrm{mm^3}$, thin along the c axis) grown using a $\mathrm{Bi_2O_3}$-based flux method were used for our experiments. Shear strain was applied on $\mathrm{ErMnO_3}$ crystals (EMO-A, B, and C) by putting a weight (alumina rod) on the crystals during a thermal treatment (see Supplemental Material, section 1 [18]). Crystals of $\mathrm{ErMnO_3}$ ($T_c = 1130\,^\circ\mathrm{C}$) were slowly cooled across the ferroelectric-trimerization transition temperature, stayed at 1140 °C for 10 min, and then slowly cooled to 1100 °C with the rate of 30 °C/h, followed by furnace cooling. In order to visualize domain patterns, crystals were etched chemically in phosphoric acid at 150 °C. The domain patterns of chemically etched crystals were observed using optical and atomic force microscopies, as phosphoric acid preferentially etches the surface of upward-polarization domains. A specimen (EMO-D) for

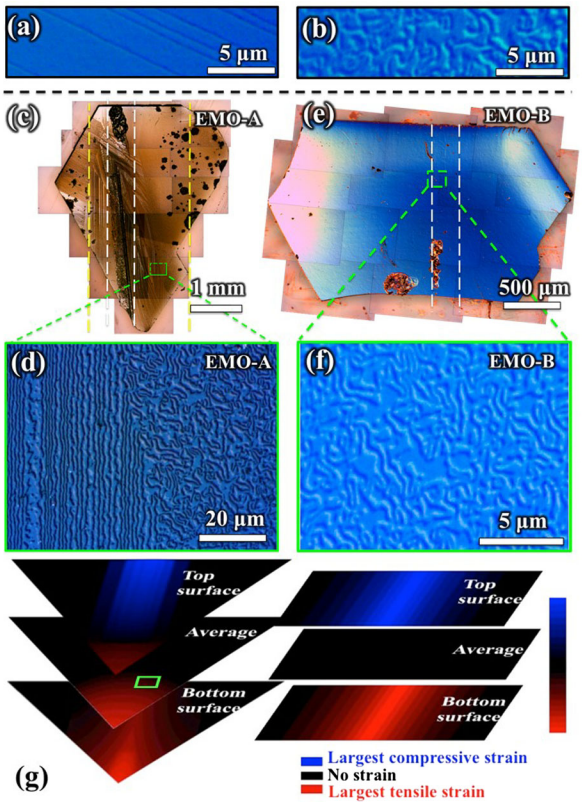

FIG. 1 (color online). Effect of the crystal shape for annealing under strain (triangle vs rectangle). (a) and (b) are OM images of chemically etched $ErMnO_3$ crystals, which indicate two distinct domain patterns: stripes and vortices. (c) Collaged optical microscope image of EMO-*A* after chemical etching. (d) Enlarged OM image of the green-box area in Fig. 1(c) showing the vortex-to-stripe transformation. (e) OM images of triangular EMO-*B*. (f) Enlarged image of the green-boxed area in Fig. 1(e) shows only vortices. (g) Schematics of in-plane strain on the top surface, average (or middle region), and bottom surface. Blue, red, and black colors indicate compressive, tensile, and no strain, respectively.

high-angle annular-dark-field scanning transmission electron microscopy (HAADF-STEM) imaging with the detection angles ranging from 68 to 280 mrad was prepared using a focused ion beam lift-out technique on a chemical-etched crystal showing the surface domain structure on the *ab* plane. HAADF-STEM images were obtained using a JEOL ARM 200 CF equipped with a CEOS Cs-corrector.

Figure 1(c) shows a low-magnification optical microscope (OM) image of the surface of an $ErMnO_3$ crystal (EMO-*A*) after applying strain at high temperatures. White dashed lines indicate the position of the alumina rod exerting a downward force on EMO-*A*. The yellow dashed lines show the location of the edges of the groove in the alumina plate (Supplemental Material, section 1 [18]). The tilted dark line between the two white lines indicates where the alumina rod touched the crystal. The rod was off centered in the vertical direction to make the force in the bottom triangular region larger than in the top region. Stripelike domains along the alumina rod direction (perpendicular to the top edge of EMO-*A*) were observed near the alumina rod, whereas the remaining area showed vortex domains. The vortex-to-stripe transformation takes place near the boundary where vortices meet stripes, as shown in Fig. 1(d), displaying a high-magnification OM image of the green-boxed area in Fig. 1(c). Vortices evidently were unfolded and became stripes. The opposite surface of EMO-*A* exhibits similar domain patterns (Supplemental Material, section 2 [18]).

In order to clarify the mechanism for the vortex-to-stripe transformation, we performed experiments on two more crystals: the rectangular-shaped $ErMnO_3$ (EMO-*B*) with a centered alumina rod [Fig. 1(e)] and another triangular-shaped $ErMnO_3$ (EMO-*C*) with an off-centered rod (Supplemental Material, section 3 [18]). Surprisingly, EMO-*B* showed only vortices with no hint of stripes, even in the region right under the alumina rod [see Fig. 1(f)], while EMO-*C* exhibited the vortex-to-stripe transformation, similar to that observed in EMO-*A*. Evidently, the crystal shape is crucial for the vortex-to-stripe transformation. Figure 1(g) shows schematically the in-plane strain distribution in triangular-shape and rectangular-shape specimens to illustrate what may be happening in those different-shape crystals (the out-of-plane strain is not shown, as it does not couple to the trimerization phase). In rectangular EMO-*B*, the top surface is compressed under the weight of the alumina rod, while the bottom surface is stretched. The top compressive and the bottom tensile strains cancel each other on average, i.e., in the middle of the crystal (See page 12 in the Supplemental Material, section 6 [18]). The triangular corner of EMO-*A* and EMO-*C* exposed to an additional strain. To amplify this effect, we intentionally shifted the center of mass of the alumina rod closer to the triangular corner, which produced an additional shear strain with a large in-plane gradient in the corner [see Fig. 1(g) and Supplemental Material, section 4 [18] for estimates of the strain magnitude, which includes Refs. [19,20]]. This average shear strain with a large gradient induces the vortex-to-stripe transformation, as discussed below.

Atomic force microscope (AFM) images, which exhibit higher spatial resolution than OM images, unveil the details of the vortex-to-stripe transformation. The AFM image of EMO-*A* in Fig. 2(a) corresponds to the optical image in Fig. 1(d). The green-boxed area in Fig. 2(a) is expanded in Fig. 2(b), and the detailed analysis of the purple-boxed area in Fig. 2(b) is shown in Fig. 2(c). There exist three trimerization domains (α, β, and γ) in h-$RMnO_3$, each supporting two directions of electric polarization. All these six domains meet to form a cloverleaf arrangement with alternating polarization direction. There are two types of cloverleaf defects with opposite sequences of domains along a loop encircling a defect, which can be viewed as vortices and antivortices. If we call the defect at the very top

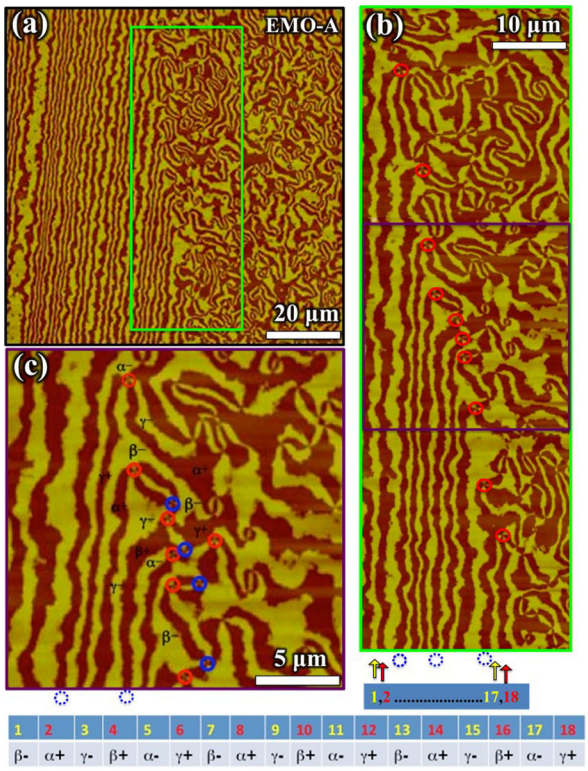

FIG. 2 (color online). (a) Large-range AFM image of the area in Fig. 1(d) showing vortex-to-stripe transformation. (b) Fine-scan AFM image of the green-boxed area in Fig. 3(a). (c) Expanded AFM image of the purple-box area in Fig. 3(b) with the self-consistently assigned trimerization and ferroelectric phases of all vortex and stripe domains. An excess of vortices (red circles, the clockwise $(\alpha-, \beta+, \gamma-, \alpha+, \beta-, \gamma+)$ sequence) at the vortex-to-stripe transformation boundary results from predominant expulsion of antivortices [dashed blue circles, the anticlockwise $(\alpha-, \beta+, \gamma-, \alpha+, \beta-, \gamma+)$ sequence]. All domain walls in stripes exhibit the same chirality corresponding to the sequence $(\alpha-, \beta+, \gamma-, \alpha+, \beta-, \gamma+)$ from right to left in the whole stripe.

of Fig. 2(c) a vortex with the sequence of the trimerized phases $(\alpha+, \beta-, \gamma+, \alpha-, \beta+, \gamma-)$ along a contour in the clockwise direction (red circle), then all cloverleaf defects in Fig. 2(c) can be labeled in a consistent manner. The resulting vortices and antivortices are marked with red and blue circles, respectively. The dark (bright) regions in AFM images display valleys (mountain plateaus) corresponding to domains with upward (downward) ferroelectric polarization [12–14].

The above analysis reveals several remarkable features: (i) the fixed sequence of the six trimerized phases $(\ldots, \alpha+, \beta-, \gamma+, \alpha-, \beta+, \gamma-, \alpha+, \beta-, \ldots)$ in the stripe region from right to left, (ii) the predominant presence of vortices at the transformation boundary (i.e., the applied strain mostly expels antivortices from the sample), and (iii) no vortices or antivortices in the stripe domain region [see Fig. 2(b) and a larger area shown in Fig. 2(a)].

The single chirality of stripes is consistent with the concept put forward by Artyukhin *et al.* [21] that an applied shear strain can stabilize a "Φ–staircase" state due to the interaction

$$F_{\text{int}} = -\lambda \int dV[(u_{xx} - u_{yy})\partial_x \Phi - 2u_{xy}\partial_y \Phi], \quad (1)$$

where u_{ij} is the strain tensor and Φ is the phase of the commensurate lattice modulation (trimerization). Equation (1) is the so-called Lifshitz invariant discussed, in particular, in the context of commensurate-incommensurate transitions [22]. In the uniform ground state $\Phi = 0$, $\pm(\pi/3)$, $\pm(2\pi/3)$ or π, corresponding to the six degenerate ferroelectric-trimerization states. Shear strain, on the other hand, favors an incommensurate lattice modulation. The compromise is the stripe state—a periodic array of parallel domain walls with Φ monotonically increasing or decreasing by $\pi/3$ at each wall (see a complete proof in the Supplemental Material, section 5 [18]).

Figure 3(a) is a schematic for Fig. 2(c), and Fig. 3(b) is a topologically deformed cartoon of transformation boundary shown in Fig. 3(a). Consider now the change of Φ along a closed yellow contour around the boundary between the topological stripe and the vortex-antivortex domains, as depicted in Fig. 3(b). According to Stoke's lemma $\oint d\mathbf{x} \cdot \nabla\Phi = 2\pi(N_V - N_A)$, where N_V and N_A are the total numbers of vortices and antivortices inside the contour, respectively. Φ changes monotonically only in the line interval AB, while in the rest of the contour Φ changes randomly. Thus, for a sufficiently large integration contour, $\Phi_B - \Phi_A = (\pi/3)N_{\text{DW}} = 2\pi(N_V - N_A)$, N_{DW} being the total number of domain walls in the stripe domain.

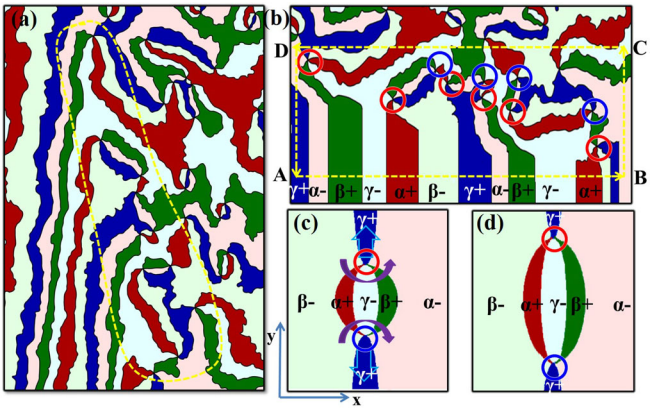

FIG. 3 (color online). (a) A schematic of Fig. 2(c). (b) A topologically deformed cartoon of the boundary between the vortex-antivortex domains (upper part) and the topological stripe domains (lower part). Vortices (antivortices) are marked with red (blue) circles. (c) A vortex-antivortex pair under the shear $u_{xx} - u_{yy}$ strain inducing vertical forces (light-blue vertical arrows) on the vortex and antivortex. Purple-curved arrows indicate the direction of the phase gradient. (d) Vertical stripe domains which are about to form, as the Magnus-type force pulls the vortex and antivortex apart.

The excess of vortices is, therefore, related to the number of stripes: one extra vortex per 6 domain walls.

The transformation of a random network of topological defects into the array of parallel stripes involves the separation of vortices from antivortices. A uniform shear strain $u_{xx} - u_{yy}$ favoring stripes along the y axis applies a force to a domain wall connecting a vortex with an antivortex. Using Eq. (1), we find that, independent from the shape of the wall, its total interaction energy is $F_{\text{int}} = -(\pi\lambda h/3)(u_{xx} - u_{yy})(y_V - y_A)$, where $y_V(y_A)$ is the y coordinate of the vortex(antivortex) and h is the sample thickness. Differentiating this energy with respect to y_V and y_A, we obtain the forces that pull the vortex and antivortex away from each other and lead to their unfolding into stripes. This process is illustrated in Figs. 3(c) and 3(d), showing a vortex-antivortex pair. The phase Φ increases in the positive x direction in the region between the vortex and antivortex, which in the presence of the strain $u_{xx} - u_{yy}$ lowers F_{int}, whereas above the vortex and below the antivortex the phase gradient has the energetically unfavorable direction. The force pulling the vortex and antivortex apart, $F_y = 2\pi\lambda h(u_{xx} - u_{yy})$, increases the length of the energetically favorable domain walls at the expense of the unfavorable ones.

One can draw an analogy between the topological stripe state and a superfluid liquid with a superfluid current proportional to the gradient of the condensate phase. The force on vortices and antivortices in h-$R\text{MnO}_3$ generated by strain is analogous to the Magnus force that moves superfluid vortices and antivortices in the direction transverse to the superfluid current (for more discussion, see Supplemental Material [18], section 6, which includes Refs. [23,24]).

If the applied uniform strain pushes all antivortices out of the sample and all vortices towards the transformation boundary, the presence of a much larger excess of vortices is be expected at the boundary, which is not consistent with our observations. Therefore, the transformation of vortices into stripes must involve an additional mechanism, which may be the coupling between vortices (antivortices) and the strain gradient due to the lattice distortion created at the vortices (antivortices) core by six merging domain walls. The resulting force pushes vortices and antivortices in the same direction (Supplemental Material, section 6 [18]). This strain-gradient-induced force can expel extra vortices and antivortices from the strained area to the outside of the specimen. This mechanism is consistent with the fact that the stripes are only observed in the regions where the strain is nonuniform.

The monochirality of stripes is confirmed by our atomic-resolution HAADF-STEM images. A scanning electron microscope (SEM) image of the top surface of EMO-D after chemical etching is shown in Fig. 4(a): narrow valleys are upward (+) polarization domains. A specimen for HAADF-STEM experiments was obtained cutting out the green-box area in Fig. 4(a) with FIB milling, and a dark-field TEM image of the specimen taken with the $(00\bar{4})$ reflection near the [100] projection shown in Fig. 4(b) displays the cross-sectional view of domain structures, which are consistent with the SEM image in Fig. 4(a). Atomic-scale HAADF-STEM experiments were performed on the domain walls labeled DW1-DW4, and false-colored HAADF-STEM images of Er-ion columns are shown in Fig. 4(c) (the full HAADF-STEM images are shown and discussed in the Supplemental Material, section 7 [18]). Kumagai and Spaldin have discussed four different types of domain walls in h-$R\text{MnO}_3$, which we label $A - D$: the A and B types have undistorted R ions at the walls, and the C and D types do not have undistorted R ions at the walls [25] (see Supplemental Material, section 8 for the schematics of the $A - D$-type domain walls [18]). The results of our HAADF-STEM experiments lead to two important findings: stripe domains are indeed monochiral (i.e., [$\alpha-$, $\beta+$, $\gamma-$, $\alpha+$, $\beta-$] along one direction), and domain walls

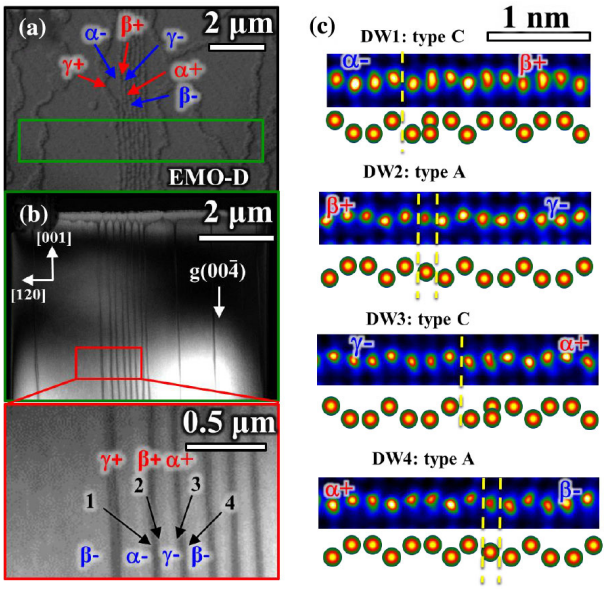

FIG. 4 (color online). STEM-HAADF analysis of different types of domain walls. (a) SEM image of EMO-D ab-plane surface after chemical etching. Mountain plateaus (valleys) are ferroelectric domains with downward (upward) polarization. The green box indicates the area cut for STEM-HAADF experiments using FIB. (b) Dark-field TEM image of a STEM-HAADF specimen with the $(00\bar{4})$ reflection near the [100] zone axis. Dark lines are narrow ferroelectric domains with upward polarization. Also shown are crystallographic axes and an enlarged image of the red box area. (c) False-colored STEM-HAADF images of 1–4 domain walls in the inset of Fig. 4(b). DW1 and DW3 domain walls are of C type (with distorted Er ions at walls), and DW2 and DW4 domain walls are of A type (with undistorted Er ions at walls). Each STEM-HAADF image is followed by schematics of Er-ion columns. C-type domain walls are slightly slanted (by a unit cell), so near the wall centers two upward and downward Er columns overlap, giving rise to elongated Er column images.

alternate between the A and C types. Although the sampling region in atomic-scale HAADF-STEM experiments is rather small, these results are fully consistent with our results discussed earlier. According to Ref. [19], the lowest energy wall is of C type. The adjacent parallel walls must then be of either A type or D type. Consistently, we find the alternation of A and C type walls. This result suggests that the domain walls around a vortex core probably exhibit the alternation of B and C types (Supplemental Material, section 9 [18]).

In summary, employing shear strain with a large gradient, we were able to transform vortices and antivortices into stripes in hexagonal $ErMnO_3$. This stripe domain state is monochiral and shows the alternation of walls with distorted and undistorted Er ions. Our findings reveal an unexpected topological relation between vortex and stripe domains in h-$RMnO_3$, and also provide a novel way of controlling topological defects. The mechanical control of topological defects in multiferroics opens a novel route to technological applications including mechanical sensors, transducers, and memories.

We thank Seung Chul Chae and Lijun Wu for fruitful discussions, and Hyeon Na Woo (RISD) for providing a three-dimensional cartoon. The work at Rutgers was supported by the National Science Foundation Grant No. DMR-1104484, and the work at Brookhaven National Laboratory was supported by the U.S. Department of Energy's Office of Basic Energy Science, Division of Materials Science and Engineering Grant No. DE-AC02-98CH10886.

*Corresponding author.
sangc@physics.rutgers.edu

[1] N. D. Mermin, Rev. Mod. Phys. **51**, 591 (1979).
[2] A. S. Logginov, G. A. Meshkov, A. V. Nikolaev, E. P. Nikolaeva, A. P. Pyatakov, and A. K. Zvezdin, Appl. Phys. Lett. **93**, 182510 (2008).
[3] E. B. Sonin, Phys. Rev. B **55**, 485 (1997).
[4] J. Bardeen and M. J. Stephen, Phys. Rev. **140**, A1197 (1965).
[5] J. D. Zang, M. Mostovoy, J. H. Han, and N. Nagaosa, Phys. Rev. Lett. **107**, 136804 (2011).
[6] E. F. Bertaut, F. Forrat, and P. H. Fang, C.R. Hebd. Seances Acad. Sci. **256**, 1958 (1963).
[7] T. Katsufuji, S. Mori, M. Masaki, Y. Moritomo, N. Yamamoto, and H. Takagi, Phys. Rev. B **64**, 104419 (2001).
[8] C. J. Fennie and K. M. Rabe, Phys. Rev. B **72**, 100103(R) (2005).
[9] B. B. Van Aken, T. T. M. Palstra, A. Filippetti, and N. A. Spaldin, Nat. Mater. **3**, 164 (2004).
[10] T. Jungk, A. Hoffmann, M. Fiebig, and E. Soergel, Appl. Phys. Lett. **97**, 012904 (2010).
[11] S. M. Griffin, M. Lilienblum, K. T. Delaney, Y. Kumagai, M. Fiebig, and N. A. Spaldin, Phys. Rev. X **2**, 041022 (2012).
[12] T. Choi, Y. Horibe, H. T. Yi, Y. J. Choi, W. D. Wu, and S. W. Cheong, Nat. Mater. **9**, 253 (2010).
[13] S. C. Chae, N. Lee, Y. Horibe, M. Tanimura, S. Mori, B. Gao, S. Carr, and S. W. Cheong, Phys. Rev. Lett. **108**, 167603 (2012).
[14] S. C. Chae, Y. Horibe, D. Y. Jeong, S. Rodan, N. Lee, and S. W. Cheong, Proc. Natl. Acad. Sci. U.S.A. **107**, 21 366 (2010).
[15] S. C. Chae, Y. Horibe, D. Y. Jeong, N. Lee, K. Iida, M. Tanimura, and S. W. Cheong, Phys. Rev. Lett. **110**, 167601 (2013).
[16] M.-G. Han, Y. Zhu, L. Wu, T. Aoki, V. Volkov, X. Wang, S. C. Chae, Y. S. Oh, and S.-W. Cheong, Adv. Mater. **25**, 2415 (2013).
[17] D. Meier, J. Seidel, A. Cano, K. Delaney, Y. Kumagai, M. Mostovoy, N. A. Spaldin, R. Ramesh, and M. Fiebig, Nat. Mater. **11**, 284 (2012).
[18] See Supplemental Material at http://link.aps.org/supplemental/10.1103/PhysRevLett.112.247601 for more discussions and details.
[19] M. Poirier, F. Laliberté, L. Pinsard-Gaudart, and A. Revcolevschi, Phys. Rev. B **76**, 174426 (2007).
[20] C. L. Lin, J. Liu, X. D. Li, Y. C. Li, S. Q. Chu, L. Xiong, and R. Li, J. Appl. Phys. **112**, 113512 (2012).
[21] S. Artyukhin, K. T. Delaney, N. A. Spaldin, and M. Mostovoy, Nat. Mater. **13**, 42 (2013).
[22] A. P. Levanyuk, S. A. Minyukov, and A. Cano, Phys. Rev. B **66**, 014111 (2002).
[23] A. Cano, A. P. Levanyuk, and S. A. Minyukov, Phys. Rev. B **68**, 144515 (2003).
[24] P. Miranović, L. Dobrosavljević-Grujić, and V. G. Kogan, Phys. Rev. B **52**, 12852 (1995).
[25] Y. Kumagai and N. A. Spaldin, Nat. Commun. **4**, 1540 (2013).